Chapter 5
Influence of Intralaminar Damage on the Delamination Crack Evolution

Cédric Huchette, Thomas Vandellos and Frédéric Laurin

5.1 Introduction

Composite laminate materials offer very interesting alternative solutions to metallic materials due to their better specific properties in numerous industrial applications and aerospace structures. Nevertheless, the design of composite structures is nowadays limited by the lack of knowledge of the damage behavior of composite materials. In the specific case of Carbon Fiber Reinforced Plastic (CFRP) laminates, it is well known that transverse matrix cracks and delamination cracks can appear early during tensile tests. It is thus necessary to propose a model that permits to predict the initiation of damage and its evolution.

Concerning delamination cracks (interlaminar damage), this kind of damage mechanism in laminated composite structures is often investigated using cohesive zone models, firstly proposed by Dugdale [29] and Barenblatt [11]. These models have the capabilities to describe the onset of a crack and its propagation even in the presence of non-linear behaviors (geometric or material). Several cohesive zone models have been developed to predict delamination in CFRP laminates [3–5, 24, 25, 68] with softening laws presenting different shapes. Whatever the model, two parameters are commonly used: the interlaminar strength, τ_0, and the critical energy release rate, also called the fracture toughness, G_c. Recent works about the characterization of the interfacial properties have demonstrated (i) the reinforcement

C. Huchette (✉) · T. Vandellos · F. Laurin
Onera—The French Aerospace Lab, 92322 Châtillon, France
e-mail: huchette@onera.fr

T. Vandellos
e-mail: thomas.vandellos@onera.fr

F. Laurin
e-mail: laurin@onera.fr

Fig. 5.1 Local delamination crack observed at the tip of the transverse matrix crack in a cross-ply laminate (detail of the crack deviation in the inset)
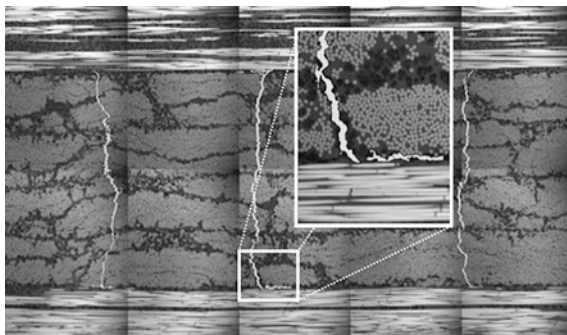
of the interfacial strengths under out-of-plane compression/shearing loadings and (ii) the influence of the mixed-mode ratio of the solicitation on the interfacial fracture toughness [12, 31, 60, 63, 73] and on the interfacial strength [18].

Even if in-ply matrix damage (intralaminar damage) is not a catastrophic failure mode for laminated composite structures contrary to delamination, the prediction of the macroscopic behavior or of the failure of composite laminates requires to take into account this damage mechanism [33]. Two kinds of approach have been developed during the last years to simulate the damage evolution (i.e. the onset of damage and its evolution). The first one is based on micromechanics models and permits to identify the relevant parameters required to finely describe the evolution of the transverse crack density in composite laminates (see Berthelot [13] for a review). This type of approach takes into account the reality of the damage pattern in order to explain the influence of the ply thickness or of the local delamination crack present at the tips of the transverse matrix cracks on the matrix crack density evolution (Fig. 5.1). The second approach is based on continuum damage mechanics [15, 44, 47, 66], which is more adapted to structure computation than micromechanics approaches. Nevertheless, the damage variables used in these models correspond to the degradation of the elastic parameters and are not necessarily correlated to the observed damage (transverse cracks, delamination crack, etc.). Moreover they do not take into account the influence of the ply thickness. Several models have thus been developed recently in order to propose a damage constitutive law at the ply level including the discrete aspect of damage and the interaction between local delamination and transverse cracking [35, 45, 67].

In composite structures subjected to various loadings such as tensile tests on open-hole plates or low velocity impact tests on laminates, for instance, intralaminar and interlaminar damage are both involved. It is thus interesting to study the influence of the transverse matrix cracks and of the associated local delamination cracks on the interlaminar damage. Wisnom and Hallett [74] explain that the final failure of open-hole plates presenting different stacking sequences is due to delamination and to the interaction between intralaminar and interlaminar damage. Guinard et al. [32] simulate the delamination induced by low-velocity impacts, taking into account the influence of the damage of each neighboring ply on the

interface under consideration. Ladevèze et al. [45] demonstrate by virtual testing that the behavior of the interface in mesomodel approaches is influenced by the damage in the adjacent plies.

The aim of this chapter is to experimentally demonstrate the influence of the intralaminar damage on the delamination evolution and to propose a model taking into account such a coupling. Section 5.2 will focus on experimental evidences which to demonstrate the influence of matrix cracking on the onset and on the propagation of the delamination cracks. Section 5.3 will propose a mesomodel approach taking into account this coupling. This model will be applied to a structural application in Sect. 5.4 in order to emphasize its contribution for the prediction of damage in laminated composites.

5.2 Influence of Intralaminar Damage on the Interlaminar Damage Evolution

5.2.1 Influence of Intralaminar Damage on Delamination Crack Onset

As mentioned in Sect. 5.1, local delamination cracks are usually observed [36] at the tips of transverse cracks in laminates (Fig. 5.1). This local delamination tends to weaken the considered interface and can lead to premature failure, due to macroscopic delamination, of composite laminated structures such as L-angle specimens. The objective of the present section is thus to demonstrate experimentally the influence of the intralaminar damages (i.e. transverse cracks and the associated local delamination cracks) on the onset of macroscopic delamination, and especially on the out-of-plane tensile strength.

5.2.1.1 Identification of the Intrinsic Out-of-Plane Tensile Strength

Different experimental tests can be found in the Ref. [53] to identify the out-of-plane tensile strength of unidirectional plies. Among these tests, the four-point bending test on L-angle specimens, proposed initially by Jackson and Ifju [38], presents a very interesting ratio between the complexity of the experimental part (manufacturing of the specimen and experimental setup) and the difficulties associated with the analysis of such a test (through analytical solutions [50] or finite element simulations). For these reasons, the four-point bending test on L-angle specimens has been normalized [9] and is currently used in design offices. The principle of such a test is illustrated in Fig. 5.2a. The two cylindrical support bars are fixed and the applied loading is imposed through the two cylindrical loading bars. This loading induces a bending moment at the curved section level, thus leading to unfold the L-angle specimen. In the case of accurately designed L-angle specimens, the observed delamination is only due to the out-of-plane tensile stress generated in the curved section, thus allowing the identification
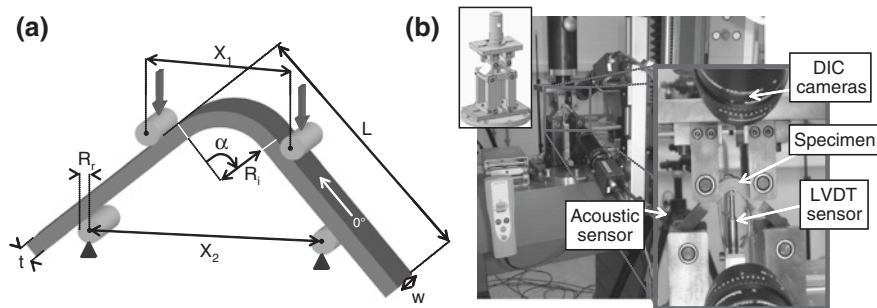
Fig. 5.2 **a** Principle of the four-point bending test on an L-angle specimen and **b** experimental device developed at Onera and the associated multi-instrumentation

of the out-of-plane tensile strength. For all the tested specimens, the propagation of the macroscopic delamination is instantaneous and instable, leading to the final failure of the specimens. This point has also been demonstrated numerically [19]. The characteristic dimensions of a L-angle specimen, also reported in Fig. 5.2a, are the total length of one leg (L), the width of the specimen (w), the total thickness (t), the internal radius of the corner (R_i) and the angle between the two legs (α). Moreover, the cylindrical bars of the four-point bending experimental device are defined by their radius (R_r) and the distances between the cylindrical loading bars (X_1) and between the cylindrical support bars (X_2). The orientation of the 0° plies in the L-angle specimens is also reported in Fig. 5.2a. The most critical parameters in the design of such a test, performed through finite element simulations, are the distances between the loading bars (X_1) and the support bars (X_2). In the present case, these geometrical parameters permit to minimize (i) the out-of-plane shear stress in the radius and in the legs and (ii) the local tensile loading in the inner radius, due to the applied bending, and to avoid transverse cracks initiation prior to macroscopic delamination.

The experimental test campaign has been performed in the framework of the STRENGTH project, under financial support of DGAC and Airbus management. The specimens have been manufactured from T700GC/M21 UD prepreg plies with a weight area of 268 g/m^2. Two different stacking sequences have been considered to identify the out-of-plane tensile strength (Z_t): (i) a thin quasi-isotropic $[45/0/-45/90]_s$ laminate (8 plies) and (ii) an intermediate disoriented $[45_2/0/-45_2/90/45/0/-45/90]_s$ laminate (20 plies). Each test is repeated three times in order to estimate the scattering.

The experimental device, developed at Onera, for the four-point bending test on L-angle specimens and the associated measurement techniques are reported in Fig. 5.2b. An electro-mechanical Schenk machine (150 kN maximum capacity) is used. The tests are performed in the machine controlled displacement mode and a constant displacement rate is imposed: 0.1 mm/min. The cylindrical bars are machined in steel and can rotate on ball bearings in order to minimize friction and thus to simplify the analysis with FE simulations. Different measurement techniques have been used to improve the understanding of the involved physical
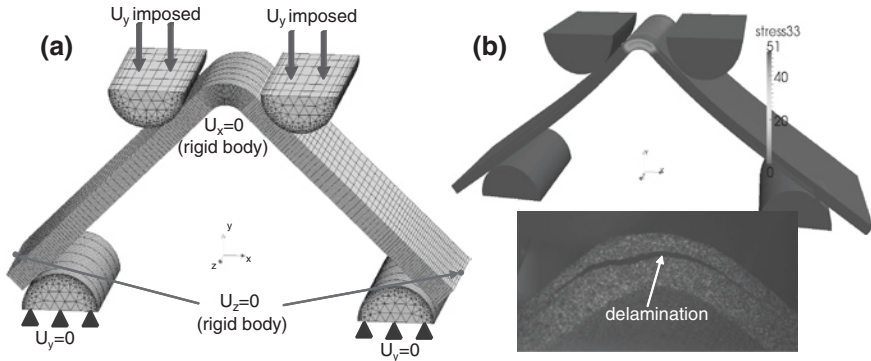
Fig. 5.3 a Mesh and boundary conditions of finite element simulations for four-point bending tests on L-angle specimens, and **b** comparison between the predicted out-of-plane stress field and the delamination pattern of a thin quasi-isotropic L-angle specimen

mechanisms and to obtain global and local informations: (i) LVDT sensor for measuring the evolution of the maximum deflection of the L-angle specimen, (ii) acoustic emission for the detection of damage events during loading, (iii) 3D Digital Images Correlation (DIC) on one free-edge of the specimen with black and white paint speckle for tracking the global displacement of the specimen and to obtain an estimate of the in-plane and out-of-plane strains and (iv) pictures taken on the other free-edge which has been properly polished in order to visualize the evolution of the intralaminar damages during the test.

The tests have been analyzed through finite element simulations in order to estimate correctly the stress field in the curved section at the failure load and to determine thus the out-of-plane tensile strength. The meshes of the studied L-angle specimens are performed using one volume linear element in the thickness of the ply. The element size is small in the curved section and under the cylindrical bars and increases in the legs to reduce the time of computation, as illustrated in Fig. 5.3a.

The boundary conditions are also reported in Fig. 5.3a. Half the loading and support bars device is meshed with volume linear elements. The displacement U_y is imposed on the upper faces of the cylindrical loading bars, while the displacement U_y of lower faces of the cylindrical support bars is fixed. Moreover, three nodes have specific conditions in order to avoid rigid body displacements of the specimen. Finally, the contact between the cylindrical bars and the specimen is taken into account while friction is assumed to be zero because of the ball bearings introduced in the experimental device. The behavior of the UD plies prior to final failure due to delamination is assumed linear elastic. This assumption is relevant in the present case since the in-plane and out-of-plane stresses remain rather low at the failure load. Moreover, no acoustic event is recorded prior to the first macroscopic delamination which confirms the absence of transverse crack before failure. Therefore, the elastic properties of the T700GC/M21 UD plies used in the present study are reported in Table 5.1. The steel cylindrical bars are assumed isotropic linear elastic with the following properties $E = 210$ GPa and $\nu = 0.3$.

Table 5.1 Material properties of the T700GC/M21 ply for the intralaminar damage constitutive law and for the cohesive zone model proposed in the present study

Type of parameters	Material properties			
Elastic properties	E_{11} (GPa)	110.0	ν_{12} (−)	0.31
	E_{22} (GPa)	8.0	G_{12} (GPa)	8.2
	ν_{23} (−)	0.40		
In-plane interfiber criterion (Eq. 5.25)	Y_t (MPa)	70.0	S_{12} (MPa)	81.0
	S_{23} (MPa)	90.0		
Effect of transverse cracks[a] (Eq. 5.21)	H_{22}^a / S_{22}^o (−)	0.67	H_{66}^a / S_{66}^o (−)	0.92
	H_{22}^b / S_{22}^o (−)	0.92	H_{66}^b / S_{66}^o (−)	1.80
	H_{22}^c / S_{22}^o (−)	2.51	H_{66}^c / S_{66}^o (−)	0.58
	H_{22}^d / S_{22}^o (−)	4.43	H_{66}^d / S_{66}^o (−)	5.69
Matrix cracking evolution law (Eq. 5.22)	α_I (−)	2.50	α_{II} (−)	0.60
	α_{III} (−)	0.60	n (−)	1
	a_h (−)	0.37	b_h (mm^{-1})	0.04
Matrix cracking threshold (Eq. 5.24)	y_I^{oE} (MPa)	0.27	y_{II}^{oE} (MPa)	0.70
	y_{III}^{oE} (MPa)	0.70		
Delay effect (Eq. 5.29)	τ_c (s)	80		
CZM stiffness (Eq. 5.6)	K (MPa mm^{-1})	10^6	α_c (−)	10^3
Out-of-plane stress criterion (Eq. 5.8)	Z_t (MPa)	51.0	S_{13}, S_{23} (MPa)	90.0
Evolution of the fracture toughness (Eq. 5.17)	G_{Ic} (J m^{-2})	340.0	G_{IIc}, G_{IIIc} (J m^{-2})	1,390.0
	κ (−)	7.4	γ (−)	3.1
	η (−)	1.6		

[a]The other components of the damage effect tensors are zero

Using finite element simulations, it is possible to determine by inverse identification the out-of-plane tensile strength which is assumed to be equal to the maximum out-of-plane tensile stress (in plane $z = 0$ in Fig. 5.3a, i.e. far from the free-edges) at the experimental failure load. As illustrated in Fig. 5.3b, for all the considered specimens, the maximum out-of-plane tensile stress is maximal at the observed failed interface which permits to validate the present identification procedure. The identified out-of-plane tensile strength is equal to $Z_t = 51\,\text{MPa}$ with a standard deviation on the six considered tests equal to 6.1 %. It is important to note that the out-of-plane tensile strength seems to be independent of the considered stacking sequences and of the total thickness of the specimen when no transverse cracking is observed prior to delamination. This point has already been demonstrated experimentally [18, 19] using the same carbon/epoxy material for many other stacking sequences and other total thicknesses (from 16 plies to 48 plies). The determined out-of-plane tensile strength seems to be an intrinsic material property which can be used in a cohesive zone model, as presented in Sect. 5.3.1.

5.2.1.2 Determination of the Influence of Intralaminar Damages on the Onset of Delamination

In the present section, the objective consists in creating transverse cracks in the L-angle specimens prior to final delamination in order to study the coupling existing between the intralaminar damages and the out-of-plane tensile strength. In order to fulfill this objective, two modifications, as compared to the previous section, have been performed. Firstly, by increasing the distances between the cylindrical bars, it is possible to enhance the local tensile loading in the lower part of the curved section which permits to generate transverse cracks in these plies prior to final delamination. Secondly, disoriented stacking sequences, containing many 90° and ±45° plies, have been chosen in order to generate more easily transverse cracks in the lower plies prior to rupture. Considering other stacking sequences than those described previously remains relevant in the present study because the out-of-plane tensile strength seems to be independent of the considered lay-up. Two different lay-ups containing 20 plies have been chosen and the stacking sequences are $[90/45/90_2/-45/0/45/90_2/-45]_s$ (noted 10/40/50 laminate) and $[45_2/90/-45_2/0/45/90/-45/0]_s$ (noted 20/60/20 laminate). For these two stacking sequences, two different distances between the cylindrical bars, determined through FE simulations, have been considered in order to generate different transverse crack densities just prior to delamination. This point is essential in order to identify and validate a model taking into account the coupling between the interlaminar and intralaminar damages in laminated composite structures. For each configuration, the test is repeated three times in order to estimate the scattering. The same experimental device and associated instrumentation as described previously have been used for all tests.

The onset and the evolution of the transverse crack density in the disoriented L-angle specimens during the tests have been monitored by different techniques in order to improve the confidence into the measurements. By monitoring the evolution of the cumulative energy, the acoustic emission permits both to detect the onset of intralaminar damages within the structure and to estimate the evolution of the crack density as reported in Fig. 5.4a. This technique permits to detect all the damage events within the structure but does not permit (i) to discriminate a transverse crack from a delamination crack and (ii) to localize the induced defects (only one sensor has been used in the present test campaign).

As a complement to the acoustic emission, analysis of pictures taken on one polished free-edge has been performed in order to distinguish the different damage mechanisms and to determine their locations. Practically, the applied displacement being maintained, some pictures are taken with a 12 bits CCD camera associated with a microscope with different objectives (×2.5 or ×5). This camera is fixed on micrometer tables thus allowing to take pictures of the different parts of the specimen edge (as reported in Fig. 5.4b). Then, these pictures are assembled to obtain a micrograph of the whole area of interest of the specimen as illustrated in Fig. 5.4b. Finally, the number of cracks is determined in each ply for the different
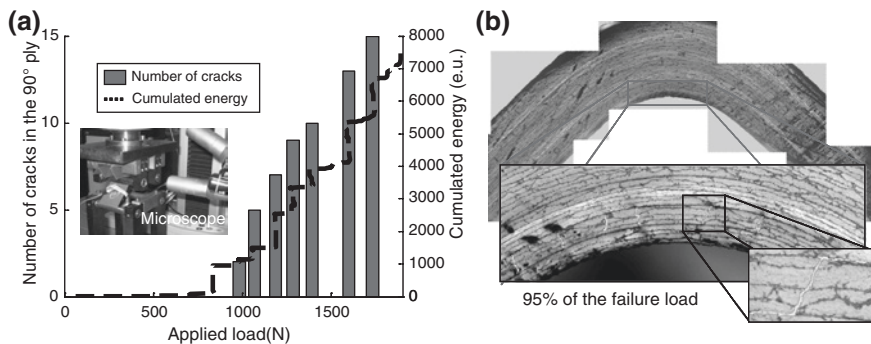
Fig. 5.4 **a** Evolution of the cumulative energy and comparison with the number of cracks detected in the lowest double 90° ply through image analysis as a function of the applied loading for a 10/40/50 L-angle specimen, and **b** visualization of the intralaminar damage pattern in the same specimen at 95 % of the failure load

load levels until the final failure which is attributed to macroscopic delamination. The pictures being taken while the structure is subjected to a bending loading, the transverse cracks are thus opened thereby permitting to detect them more easily. Moreover, local delamination cracks are clearly observed at the tips of the transverse cracks located in the lower plies such as the lowest double 90° plies for the 10/40/50 specimen presented in Fig. 5.4b. It is also worth mentioning that the pictures have been taken as a function of the monitored acoustic events to optimize the monitoring of such a test. Finally, the evolution of the crack density has been compared successfully with the discontinuities observed in the cumulative energy recorded by acoustic emission for the different tested configurations, as presented in Fig. 5.4b for a 10/40/50 specimen.

Moreover, the analysis of the strain fields measured by stereo-digital images correlation can also permit to detect mesoscopic intralaminar cracks in the structure as proposed in [48]. Indeed, when transverse cracks are initiated during loading, a discontinuity is induced in the displacement field and the cracks can be detected using the strain obtained through derivation of the displacement field. The evolution of the crack density can thus be automatically measured and has been successfully compared with the other measurement techniques permitting to improve the confidence in the available experimental data. It can be noted that for the four considered cases (two different geometrical configurations for two different stacking sequences), the measured transverse crack densities just prior to final failure are notably different which should permit to identify the inter/intralaminar damage coupling parameters of a damage model as the one described in Sect. 5.3.3.

For the considered damaged L-angle specimens, the observed failure pattern is drastically different from that observed on specimens in which no transverse cracking is observed prior to delamination. Indeed, as presented in Fig. 5.5a, for a 20/60/20 specimen containing no intralaminar damage prior to final failure (stacking sequence presented in Sect. 5.2.1.1), only the mostly loaded interface,
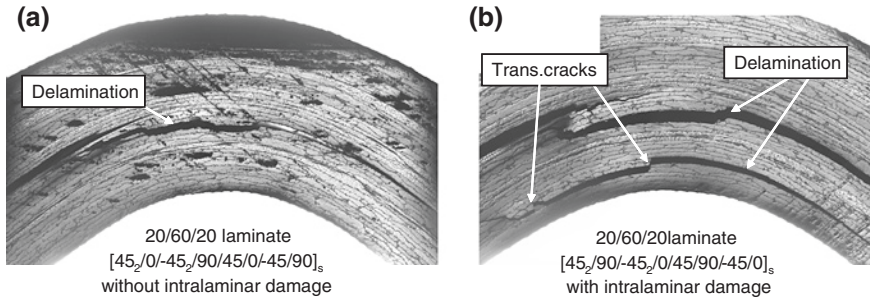
Fig. 5.5 a Failure pattern of the disoriented 20/60/20 specimen without intralaminar damage prior to delamination, and **b** failure pattern of the disoriented 20/60/20 specimen with intralaminar damage prior to delamination

located at the mid-thickness of the specimen, failed and led to the final failure of the specimen. Nevertheless, in the present disoriented laminate (in which the positions of the 0° plies have been permuted with those of the 90° plies as compared to the previous lay-up), two main delamination cracks are observed in Fig. 5.5b. The mostly loaded interface still failed but a delamination crack is also observed in the interface between the damaged 45° and 90° plies located near the inner radius. A clear interaction is observed between the transverse cracks in the lowest 90° ply and the delamination crack. The local delamination cracks at the tips of the transverse cracks weaken the interface located between the intralaminar damaged plies and lead to the premature failure of the specimens while the applied out-of-plane stress at this interface remains markedly lower than the out-of-plane tensile strength. The same failure pattern, consisting in several delamination cracks in the interfaces between the damaged plies located near the inner radius, is observed on the other tested stacking sequences and the interaction between the different damage mechanisms is also visible.

Therefore, it has been demonstrated, in this section, that the failure patterns of L-angle specimens are modified due to the presence of intralaminar damages (especially due to the local delamination cracks located at the tips of the transverse cracks). In the present study, these experimental evidences suggest that it is essential to introduce coupling between the onset of delamination and intralaminar damages.

5.2.2 Influence of Intralaminar Damage on Delamination Crack Propagation

It is generally admitted that delamination must be characterized by an onset criterion and a propagation criterion. The propagation criterion represents the evolution of the fracture toughness, i.e. the energy release rate needed to propagate a crack at

the interface, as a function of the mixed-mode ratio often defined as $G_{II}/(G_I + G_{II})$ with G_I (resp. G_{II}) the energy release rate for mode I (resp. mode II). The characterization of the propagation criterion is based on many fracture tests such as the double-cantilever beam (DCB) and the end-notched flexure (ENF) tests for toughness in modes I and II [7, 14, 27, 28, 54, 64, 65]. As a mixed-mode is more likely to occur in structures subjected to in service loadings, several experiments have been developed such as the mixed-mode flexure (MMF) test and the mixed-mode bending (MMB) test allowing a mixed-mode characterization. The MMB test is the most commonly used because it allows investigating all mixed-mode ratios between modes I and II [7, 21, 26, 55, 56, 61, 62]. However, these tests are classically performed on unidirectional (UD) $[0°]_n$ laminates whereas most composite structures subjected to complex loadings involve multidirectional (MD) laminates where delamination fracture mainly occurs in the interfaces between the differently oriented plies. Therefore an increasing amount of researches is devoted to the evaluation of the fracture toughness of MD laminate interfaces [6, 20, 26, 55, 56, 59, 60]. However, one of the major problems in testing those MD specimens is the presence of intralaminar damage. Indeed, with the commonly used fracture tests, this kind of damage is difficult to quantify and its influence on the characterization of the energy release rate during delamination crack growth is also difficult. However this coupling between intralaminar damage and delamination is crucial in order to describe the damage scenario of composite materials in structures. Consequently, a new fracture test, adapted to MD laminate interfaces, has been proposed recently [71]: the Tensile Flexure test on Notched Specimen (TFNS test).

5.2.2.1 The Tensile Flexure Test on Notched Specimen

Description of the Experimental Procedure

In order to characterize the propagation of delamination in $\pm\theta°$ plies of unidirectional continuous fiber laminates, a new experimental procedure, based on fracture mechanics, has been proposed. The aim of this new test, called Tensile Flexure test on Notched Specimen (TFNS test), is to determine the fracture toughness of a $0°/\theta°$ interface. In order to study the delamination of the $0°/\theta°$ interface, the most appropriate staking sequence is $[0_n/\pm\theta_m]_s$. This test procedure is divided into three steps (Fig. 5.6).

In the first step, a notch is machined in the top $0°$ plies of the laminate in the middle of the specimen in order to introduce a local tensile/bending coupling in the laminate behavior.

The second step is devoted to the specimen preparation (i.e. the initiation of the delamination crack). The tensile loading is applied in a displacement controlled mode for the sake of crack propagation stability. The tensile loading leads to the initiation of a transverse crack under the notch through the $\pm\theta°$ plies. This transverse crack finally reaches the last $0°/\theta°$ interface, leading to

Fig. 5.6 Experimental procedure of the tensile flexure test on notched specimen
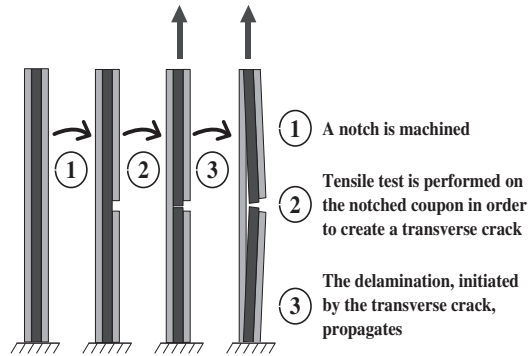
local delamination through crack deflection in this interface. Once the local delamination has occurred in the $0°/\theta°$ interface, the specimen is unloaded.

After these two steps, the third step concerns the propagation of the delamination crack front initiated in the $0°/\theta°$ interface on both sides of the transverse crack. The propagation of delamination is thus investigated through a second tensile test. The load, the displacement and the delamination lengths are recorded in order to calculate the fracture toughness. It is worth mentioning that, contrary to other fracture mechanics tests, the delamination occurs without the presence of a Teflon® insert as in the test proposed by O'Brien [52]. However, with the TFNS test, the delamination crack is not created by free edge effects (as in [52]), the control of which is very difficult, but results from the deviation of the transverse crack from the $\theta°$ ply into the $0°/\theta°$ interface.

Description of the Experimental Device

The TFNS test was performed on an electromechanical testing machine, equipped with a 150 kN load cell, operating in a displacement controlled mode. A digital video microscope is used to observe the damage state at the ply scale (mesoscopic scale) and at the fiber/matrix scale (microscopic scale). This microscope, which is fixed on micrometric displacement tables (Fig. 5.7), allows the measurement of the length of the delamination crack. Numerous displacement plateaus are imposed (every 0.04 mm) thus allowing an accurate observation of the propagation of the delamination crack under loading. The displacement, applied to the specimen, is determined by the variation of the length of the specimen measured during the test at each displacement plateau.

The T700GC/M21 laminate has been chosen because it is a 3rd generation carbon/epoxy material which exhibits a high fracture toughness and experimental results obtained using other experimental devices are available in the literature [60].

The length of the coupon is 100 mm whereas its width is 12 mm. The thickness of the coupon and the notch depth in the middle of the specimen depend on the stacking sequence of the laminate. For instance, in a $[0_n/90_m]_s$ specimen, the
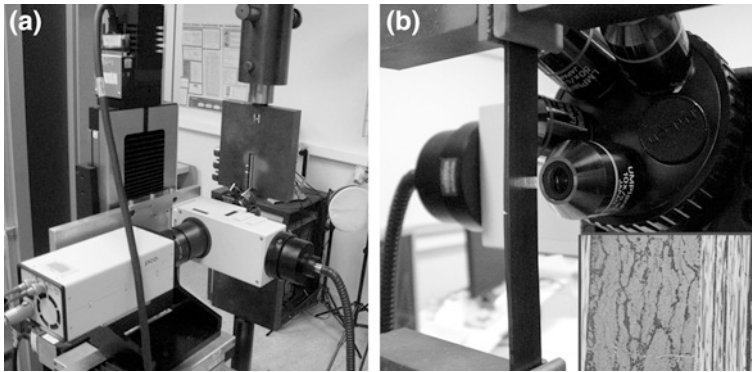
Fig. 5.7 Experimental device: **a** the digital camera fixed on the displacement tables, and **b** micrograph of the sample (inset) during testing provided by the microscopic head of the digital camera

notch depth must be superior to the thickness of the 0° plies since it is essential to avoid that the crack initiates and propagates in the top 0° plies but propagates as a transverse crack in the 90° plies and thus attains the other 0°/90° interface in order to deviate in this interface, thus leading to delamination.

Experimental Observations

The evolutions of stress and of crack length versus the imposed displacement for several coupons demonstrate the good reproducibility of the TFNS, as shown in Fig. 5.8 for four $[0_2/90_2]_s$ T700GC/M21 carbon/epoxy specimens. Moreover, the crack growth is stable, without any damage in the plies, as long as the delamination length is short enough (i.e. 1/3 of the total length of the specimen).
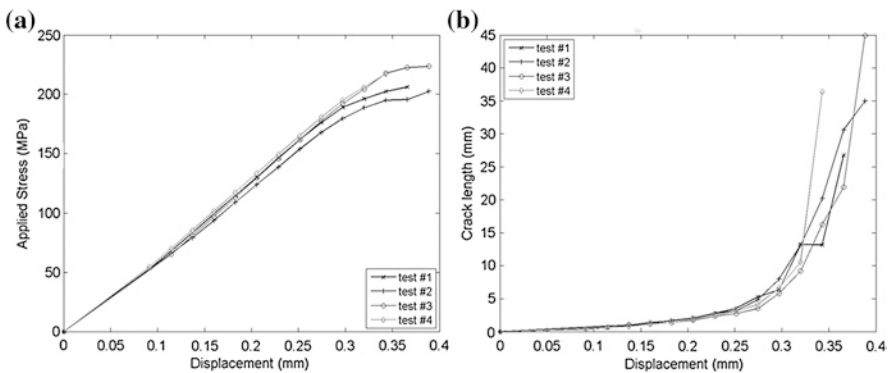

Fig. 5.8 **a** Stress versus imposed displacement, and **b** crack length versus imposed displacement for several TFNS tests on $[0_2/90_2]_s$ T700GC/M21 carbon/epoxy laminates

Besides, the delamination crack consists in two cracks propagating with a quasi-symmetrical behavior. It is worth mentioning that the stress-displacement curve is not linear. This behavior is due to the presence of the notch which leads to bending of the specimen under tensile loading.

Identification of the Interface Toughness in a T700GC/M21 Carbon/Epoxy Laminate

From five TFNS tests on $[0_2/90_2]_s$ specimens and two tests on $[0_3/45/-45]_s$ specimens of T700GC/M21 carbon/epoxy laminate, fracture toughness identification was performed using the Modified Virtual Crack Closure Technique (MVCCT) method [43], based on the Linear Elastic Fracture Mechanics. Due to bending of the laminate observed during the tensile test, the calculation assumption of large displacements is made. Using the applied load or the applied displacement measured during the experiment and the measured delamination lengths, it is possible to simulate the experimental conditions and to use this technique to identify the fracture toughness. The application of the MVCCT method on the TFNS test indicates a mixed-mode ratio $G_{II}/(G_I + G_{II})$ evolving with the crack growth.

The results presented in Fig. 5.9 show (i) that the mixed mode evolves from 15 to 35 % of mode II with the $[0_2/90_2]_s$ specimen and from 35 to 45 % of mode II with the $[0_3/45/-45]_s$ specimen and (ii) that the fracture toughness increases as a function of the mixed-mode ratio which increases to 1 (mode II). It should be noted that such results are in good agreement with those reported in Refs. [12, 59]. Moreover, it is worth mentioning that contrary to other tests, the mixed-mode ratio changes. Therefore, the TFNS test permits to obtain, with only one test, the evolution of the fracture toughness of MD laminate interfaces as a function of the mixed mode ratio. The propagation criterion (Eq. 5.17) can be identified using these data (Fig. 5.9).

Fig. 5.9 Identification of a propagation law (Eq. 5.17) based on the fracture toughness identified by MVCCT from the TFNS tests
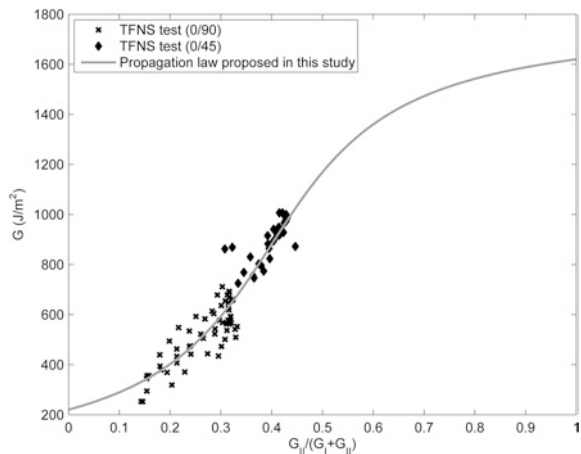
5.2.2.2 Demonstration of the Influence of Intralaminar Damage on the Interfacial Fracture Toughness

The influence of intralaminar damage on the onset of delamination has been proved in Sect. 5.2.1.2. It seems obvious that the value of the fracture toughness of the interface is also influenced by the intralaminar damage (transverse matrix cracking, local delamination) but its identification remains difficult.
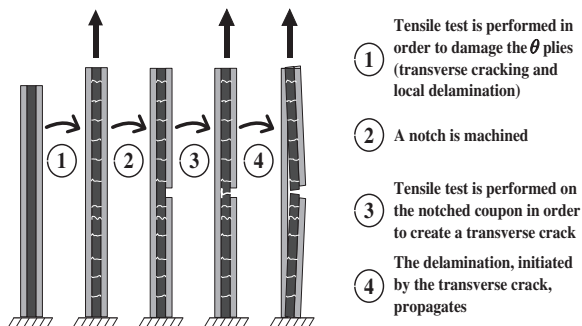
Adding a new step at the beginning of the experimental procedure of the TFNS test, it is possible to study the intralaminar damage effect on the propagation of the delamination crack. Indeed, using a tensile test on the laminated specimen without notch, several transverse cracks are created in the $\theta°$ plies. The initial experimental procedure is then followed as shown in Fig. 5.10.

It is important to note that the transverse crack density does not change during the tensile test on the notched specimen. Besides, it is possible to observe the influence of the transverse crack density on the propagation of the delamination crack in the 0°/90° interface. Moreover, it is worth mentioning that the experimental device used during the test permits to evaluate, for each displacement plateau, the length of the delamination crack, the number of transverse cracks in the specimen and the length of the local delamination cracks present at the tips of the transverse cracks.

As shown in Fig. 5.11 for several stacking sequences, the transverse cracking rate (i.e. the number of transverse cracks from one unit of length) and the average length of the local delamination depend on the level of the applied stress during the first tensile test. In order to obtain a good compromise, during the TFNS test, between the number of transverse cracks and the length of local delamination cracks, the stacking sequence $[0_2/90_2]_s$ has been chosen.

In order to identify the influence of the level of intralaminar damage on the propagation of the delamination crack, five damage states have been studied. The comparison of the curves representing the evolution of the applied stress as a function of strain shows that the initial slope can not be associated with the different levels of intralaminar damage under consideration. Nevertheless, when the damage level increases, the rigidity seems to decrease sooner (Fig. 5.12a). Moreover, the evolution of the normalized crack length versus strain clearly shows that the

Fig. 5.10 Experimental procedure of the tensile flexure test on notched specimen for studying the influence of intralaminar damage on the propagation of delamination
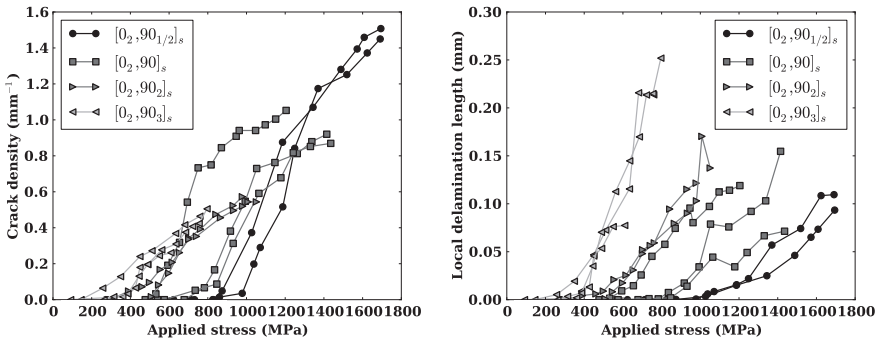
1. Tensile test is performed in order to damage the θ plies (transverse cracking and local delamination)

2. A notch is machined

3. Tensile test is performed on the notched coupon in order to create a transverse crack

4. The delamination, initiated by the transverse crack, propagates

Fig. 5.11 Evolution of the number of transverse cracks by millimeter and of the average local delamination length as a function of the applied stress for several cross-ply T700GC/M21 laminates

propagation of the delamination crack occurs earlier when the intralaminar damage level increases (Fig. 5.12b). Nevertheless, due to the fact that the experimental curves, obtained with intralaminar damage, are included into the dispersion of the experimental curves without intralaminar damage, the identification of the fracture toughness as a function of the intralaminar damage level is not possible.

However, according to numerical simulations of the TFNS test, the effect of the intralaminar damage level on the fracture toughness seems to be realistic. Indeed, the more the fracture toughness of the cohesive zone model (described in Sect. 5.3.1 and used to describe the propagation of the delamination crack at the 0°/90° interface during the TFNS test) decreases, the more the propagation of the crack occurs earlier (Fig. 5.13), as observed during the experimental tests. Therefore, it seems obvious that the fracture toughness has to be influenced by the intralaminar damage level.
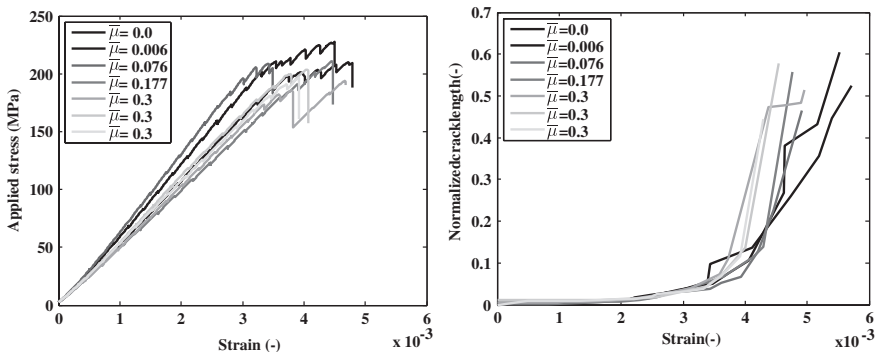

Fig. 5.12 Evolution of the applied stress and normalized crack length as a function of strain for several levels of intralaminar damage obtained from TFNS test on $[0_2/90_2]_s$ T700GC/M21 carbon/epoxy specimens
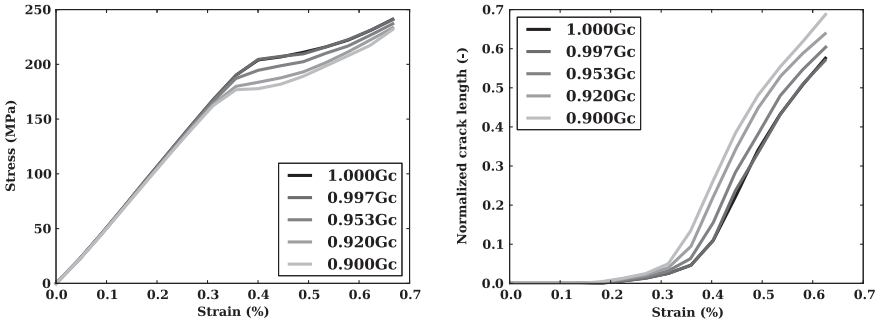
Fig. 5.13 Evolution of the applied stress and the normalized crack length versus strain obtained by the simulation of the TFNS test with several values of the fracture toughness

5.3 Modeling the Effect of Intralaminar Damage on the Interlaminar Damage Evolution

5.3.1 Cohesive Zone Model for Modeling the Interlaminar Damage

5.3.1.1 General Framework of the Cohesive Zone Model

Cohesive zone models are generally used to describe the behavior of interfaces. More precisely, the tractions T_i between the top and bottom surfaces of the interface are related to the relative displacements δ_i, with $i = 1 - 3$ (Fig. 5.14). The value $i = 1$ corresponds to the opening mode of fracture (mode I) whereas the values $i = 2$ and $i = 3$ are related to the shearing modes (mode II and mode III).

In the general framework, the constitutive law can be written as

$$\text{if } \delta_1 \geq 0 \quad \text{if } \delta_1 < 0$$
$$\begin{cases} T_1 = K \, \delta_1 f(\lambda) \\ T_i = K \, \delta_i f(\lambda) \end{cases} \begin{cases} T_1 = \alpha_c \, K \, \delta_1 \\ T_i = K \, \delta_i f(\lambda) \end{cases} \quad \text{with } i = 2, 3 \tag{5.1}$$

where δ_1 (respectively δ_2 and δ_3) is the relative displacement in mode I (respectively in mode II and III), T_1 (respectively T_2 and T_3) is the traction force in mode I (respectively in mode II and mode III), K is the initial stiffness of the interface (considered, in this work, as being the same whatever the fracture mode), α_C is a penalization factor for out-of-plane compression, λ is the damage variable, related to the damage kinetics, and $f(\lambda)$ represents the effect of damage. As proposed in [19], the damage variable λ can be then defined from the relative displacement δ and the material parameters δ_0 and δ_f. The relative displacement δ is determined by

$$\delta = \sqrt{\langle \delta_1 \rangle_+^2 + \delta_2^2 + \delta_3^2} \tag{5.2}$$

Fig. 5.14 The constitutive
law in single-mode loading
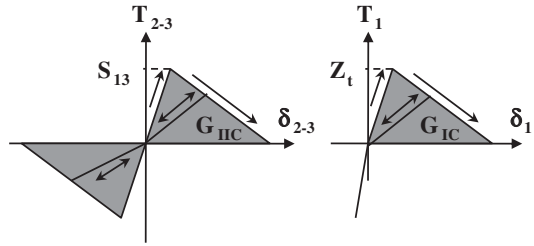
where $\langle \cdot \rangle_+$ are the classical Macaulay brackets defined by

$$\langle x \rangle_+ = \max[0, x] \tag{5.3}$$

It should be noted that, in order to avoid damage under pure out-of-plane compressive normal stress, the normal relative displacement δ_1 is only taken into account in the relative displacement δ when positive. As illustrated in (Fig. 5.15), δ_0 is the relative displacement associated with the damage threshold τ_0 and the interfacial stiffness K, and δ_f is the relative displacement attained when the energy release rate G is equal to the fracture toughness G_c (corresponding to the area under the constitutive law for a constant mixed-mode ratio).

δ_f depends on the shape of the cohesive zone law and on the fracture toughness G_c. It is calculated, for a constant mixed-mode ratio, by

$$G_c = \int_0^{\delta_f} T(\delta) \mathrm{d}\delta \tag{5.4}$$

where the value of G_c is experimentally identified by fracture tests. Therefore, the general framework for the definition of a cohesive zone model depends on

- $f(\lambda)$ which represents the damage effect,
- the damage evolution law which is associated with the damage variable λ,
- δ_0, determined from an onset criterion (i.e. the evolution of the interfacial strength τ_0 as a function of the mixed-mode ratio),
- δ_f, defined using a propagation law (i.e. the evolution of the interfacial toughness G_c as a function of the mixed-mode ratio).

Fig. 5.15 A bilinear
constitutive law for
a mixed-mode solicitation
according to [16]
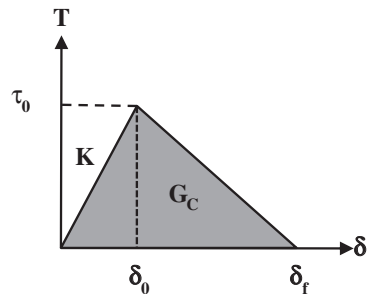
5.3.1.2 Damage Evolution Law of the Interlaminar Damage

The proposed framework permits to develop a cohesive zone model based on the experimental characterization and using any shape of law including an elastic part. The bilinear law is implemented in various finite element codes and has been used successfully by different authors [16, 69, 70]. However, questions concerning the influence of the shape of the law on the results and on the convergence (when a quasi-static implicit finite element code is used) are often raised. The tri-linear model presented here is more flexible than the bilinear one and permits to overcome some of its drawbacks [72].

As presented in Fig. 5.16, two parts could be distinguished in the model: a first one (from τ_0 to $\tau^\star$) in which the released energy is equal to ω_1 and a second one (from $\tau^\star$ to 0) in which the released energy is equal to ω_2. τ_0 is the strength of the interface for a given mixed-mode ratio. $\tau^\star$ is the maximal damageable stress which represents the admissible stress on the interface at the end of the first part of the damage process. $\tau^\star$ is defined by $\tau^\star = \alpha_\sigma \tau_0$ where α_σ is a shape parameter which is generally a constant (if $\alpha_\sigma = 1$ the shape is trapezoidal). The total energy released during the damage process is equal to G_c with $G_c = \omega_1 + \omega_2$ ($\omega_1 = \alpha_G G_c$). It should be noted that τ_0 and G_c are respectively defined by the initiation criterion and the propagation law experimentally identified (Sect. 5.2).

The evolution of the damage variable is defined by Eq. 5.5 and the damage behavior by Eq. 5.6.

$$\begin{cases} \lambda = 0 & \text{if } \delta \leq \delta_0 \\ \lambda = (\delta_0 - \delta)\frac{\delta^\star - \alpha_\sigma \delta_0}{\delta(\delta_0 - \delta^\star)} & \text{if } \delta_0 < \delta \leq \delta^\star \\ \lambda = \min\left[\frac{\delta(\delta^\star - \delta_f) + \alpha_\sigma \delta_0(\delta_f - \delta)}{\delta(\delta^\star - \delta_f)}, 1\right] & \text{if } \delta \geq \delta^\star \\ \dot{\lambda} \geq 0 \end{cases} \tag{5.5}$$
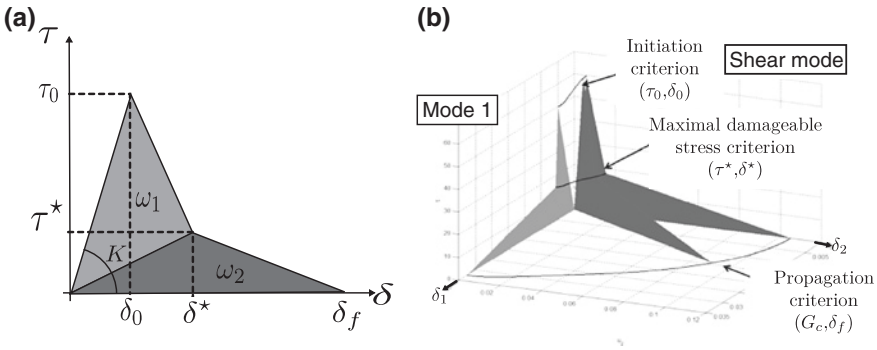

Fig. 5.16 Shape of the tri-linear model **a** for a constant mixed-mode ratio in the (δ, τ) plane, and **b** for mixed-mode ratios between mode I and shear mode

$$\text{if } \delta_1 \geq 0 \qquad \text{if } \delta_1 < 0$$
$$\begin{cases} T_1 = K(1-\lambda)\delta_1 \\ T_i = K(1-\lambda)\delta_i \end{cases} \begin{cases} T_1 = \alpha_c K\delta_1 \\ T_i = K(1-\lambda)\delta_i \end{cases} \quad \text{with } i = 2,3 \qquad (5.6)$$

$\delta_0, \delta^\star, \delta_f$ are material parameters corresponding to the initiation criterion (δ_0) and to the propagation law ($\delta^\star, \delta_f$). These parameters are defined by

$$\begin{cases} \delta_0 = \frac{\tau_0}{K} \\ \delta_f = 2\frac{\omega_2}{\tau^\star} \\ \delta^\star = \delta_0 + \alpha_\delta(\delta_f - \delta_0) \quad \text{with } \alpha_\delta = \frac{G_c - 12\tau_0\delta_0}{12\tau_0(\delta_f - \delta_0)} - \alpha_\sigma \end{cases} \qquad (5.7)$$

5.3.1.3 Determination of the Onset Criterion with Reinforcement of the Interfacial Strengths Under Out-of-Plane Compression/ Shearing Loadings

The recent work of Charrier et al. [18] has demonstrated the reinforcement of the interfacial strength under out-of-plane compression/shearing solicitations. In order to model this reinforcement, the concept of a positive part of the stress tensor has been used. The concept of this kind of formulation is the determination of the stresses, in the plane of the crack, which are only responsible for the damage, following the procedure proposed in [39]. Besides, the onset criterion can be written as

$$\left(\frac{\sigma_{33}^+}{Z_t}\right)^2 + \left(\frac{\tau_{13}^+}{S_{13}^c}\right)^2 + \left(\frac{\tau_{23}^+}{S_{23}^c}\right)^2 = 1 \qquad (5.8)$$

where Z_t is the through-thickness tensile strength identified using a four-point bending test on L-angle laminates (Sect. 5.2.1.2), S_{13}^c and S_{23}^c are the positive shear strengths. $\sigma_{33}^+, \tau_{13}^+$ and τ_{23}^+ are the positive interlaminar stresses defined, following [39], by

$$\begin{cases} \sigma_{33}^+ = \frac{(\lambda^+)^3}{\Omega} \\ \tau_{13}^+ = \frac{\tau_{13}(\lambda^+)^2}{\Omega} \\ \tau_{23}^+ = \frac{\tau_{23}(\lambda^+)^2}{\Omega} \end{cases} \quad \text{with } \begin{cases} \lambda^+ = \frac{\left(\sigma_{33} + \sqrt{\sigma_{33}^2 + 4(\tau_{13}^2 + \tau_{23}^2)}\right)}{2} \\ \Omega = (\lambda^+)^2 + (\tau_{13}^2 + \tau_{23}^2) \end{cases} \qquad (5.9)$$

Positive normal σ_{33}^+ and shear τ_{13}^+ stresses are generated using Eq. 5.9, even under pure shear loading (τ_{13} for instance). In order to respect the identified interlaminar strengths under pure shear loading, the positive shear strengths S_{13}^c and S_{23}^c are defined by

$$S_{13}^c = \frac{S_{13}}{2\sqrt{1 - \left(\frac{S_{13}}{2Z_t}\right)^2}} ; \; S_{23}^c = \frac{S_{23}}{2\sqrt{1 - \left(\frac{S_{23}}{2Z_t}\right)^2}} \qquad (5.10)$$

Fig. 5.17 Comparison between the quadratic criterion classically used and the criterion with reinforcement
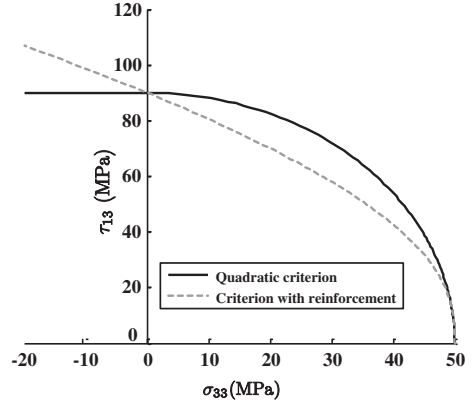
where S_{13} is the interlaminar strength in mode II (identified using Interlaminar Shear Strength (ILSS) tests on 0° unidirectional (UD) plies [10]) and S_{23} is the interlaminar strength in mode III (identified using ILSS tests on cross-ply laminates [18]). Figure 5.17 shows the difference between the present criterion and the classically used quadratic criterion [22].

For convenience, before onset of failure, the tri-axial stress state is represented using the relative displacement. Thus, the part of the participation of each through-thickness stress is defined using two parameters

$$\begin{cases} \theta = \arccos\left(\frac{\delta_1}{\delta^{\text{eq}}}\right) \\ \omega = \arctan\left(\frac{\delta_3}{\delta_2}\right) \end{cases} \tag{5.11}$$

where ω represents the participation of the interlaminar shear stress in mode III compared with the interlaminar shear stress in mode II and θ the participation of the interlaminar normal stress compared with the interlaminar shear stress. The magnitude of the total relative displacement is defined by

$$\delta^{\text{eq}} = \sqrt{\delta_1^2 + \delta_2^2 + \delta_3^2} \tag{5.12}$$

It should be noted that, compared with the relative displacement δ defined in Eq. 5.4, the total relative displacement takes into account the normal relative displacement, even if it is negative, in order to take into account the effect of the out-of-plane compressive stress on the onset criterion.

Assuming that the stiffness K is the same whatever the loading direction, and reporting Eqs. 5.9 and 5.11 in Eq. 5.8, then the relative displacement at initiation δ_0 is given by

$$\delta_0 = \frac{\delta_0^\star}{\sqrt{a_{33}^2 + a_{13}^2 + a_{23}^2}} \tag{5.13}$$

with

$$
\begin{cases}
a_{33} = \dfrac{\tilde{a}^3}{\tilde{a}^2 + \sin^2 \theta} \\[2mm]
a_{13} = \dfrac{\tilde{a}^2 \sin \theta \cos \omega}{\tilde{a}^2 + \sin^2 \theta} \dfrac{Z_t}{S_{13}^c} \\[2mm]
a_{23} = \dfrac{\tilde{a}^2 \sin \theta \sin \omega}{\tilde{a}^2 + \sin^2 \theta} \dfrac{Z_t}{S_{23}^c} \\[2mm]
\tilde{a} = \frac{1}{2} \left(\cos \theta + \sqrt{\cos^2 \theta + 4 \sin^2 \theta} \right) \\[2mm]
\delta_0^\star = \dfrac{Z_t}{K}
\end{cases}
\tag{5.14}
$$

The evolution of the fracture toughness G_c as a function of the mixed-mode ratio is experimentally characterized using fracture tests [7, 8, 14, 17, 21, 27, 28, 37, 51, 57, 62–65]. This evolution is classically defined by a propagation law such as the power law (Eq. 5.15)

$$
\left(\frac{G_I}{G_{Ic}} \right)^\alpha + \left(\frac{G_{II}}{G_{IIc}} \right)^\alpha + \left(\frac{G_{III}}{G_{IIIc}} \right)^\alpha = 1
\tag{5.15}
$$

in which α is a material parameter or the Benzeggagh law (Eq. 5.16)

$$
\begin{cases}
G_c = G_{Ic} + (G_{IIc} - G_{Ic})B^\eta \\[2mm]
B = \dfrac{G_{II} + G_{III}}{G_I + G_{II} + G_{III}}
\end{cases}
\tag{5.16}
$$

where η is a material parameter. Nevertheless, the evolution of the fracture toughness as a function of the mixed mode ratio identified by TFNS tests (Sect. 5.2.2.2) is not well described by the precedent propagation laws. In this respect, Vandellos et al. [71] have proposed an improved propagation criterion (Eq. 5.17).

$$
\begin{cases}
G_c = G_{Ic} + (G_{IIc} - G_{Ic})B^\eta \\[2mm]
B = \dfrac{\arctan \left(\frac{\kappa G_{II}}{G_I + G_{II} + G_{III}} - \frac{\kappa}{\gamma} \right) - \arctan \left(-\frac{\kappa}{\gamma} \right)}{\arctan \left(\kappa - \frac{\kappa}{\gamma} \right) - \arctan \left(-\frac{\kappa}{\gamma} \right)}
\end{cases}
\tag{5.17}
$$

in which η, κ, γ are material parameters. A comparison between the identified parameters of this proposed criterion and the experimental data is presented in Fig. 5.9 thereby evidencing a good agreement between the propagation law predictions and the experimental data for the T700GC/M21 carbon epoxy material (see the parameter values in Table 5.1).

Following the definition proposed in [58], the local mixed-mode ratio is defined by

$$
\begin{cases}
\beta = \arccos \left(\frac{\delta_1}{\delta} \right) \\[2mm]
\omega = \arctan \left(\frac{\delta_3}{\delta_2} \right)
\end{cases}
\tag{5.18}
$$

Thus, the energy release rates related to the fracture modes are given by

$$\begin{cases} G_I = G_c \cos^2 \beta \\ G_{II} = G_c \sin^2 \beta \cos^2 \omega \\ G_{III} = G_c \sin^2 \beta \sin^2 \omega \end{cases} \tag{5.19}$$

Using Eq. 5.4, an analytical relation can be expressed between the fracture toughness and the maximal admissible displacement δ_f. For instance, this equation for the tri-linear model is

$$\delta_f = \frac{G_c - 1/2\tau_0\delta_0}{1/2\tau_0(\alpha_\delta + \alpha_\sigma)} + \delta_0 \tag{5.20}$$

Thus, reporting in this relation the value of the fracture toughness obtained from the propagation law, the maximal admissible displacement δ_f is evaluated.

5.3.2 Damage Evolution Law of Intralaminar Damage

Section 5.2 has demonstrated the influence of matrix cracking on the evolution of the delamination crack. Although micromechanics studies [13] have shown the important effect of the local delamination on the saturation of the transverse cracking, only a few continuum damage models [23, 35, 45, 46] take into account the evolution of these two types of matrix damage.

To be able to take into account the influence of intralaminar damage on the delamination evolution, a simplified version of the multiscale hybrid approach for the damage prediction until the final failure of laminated composites developed by Laurin et al. [46] is proposed to simulate the evolution of transverse matrix cracking and local delamination. In this model, two damage variables are used to describe the matrix damage behavior of each ply: $\overline{\rho}$ (the normalized crack density, i.e. the crack density multiplied by the thickness of the considered ply) and $\overline{\mu}$ (the local delamination ratio, i.e. the total length of local delamination cracks divided by the total length of the interface). In order to develop a mesoscopic damage law, it is first necessary to identify the effect of the damage on the stiffness of the damaged ply. Nevertheless, it is very difficult to determine experimentally the stiffness reduction of a cross-ply laminate with a sufficient accuracy, especially for carbon/epoxy composites. Consequently, a numerical approach based on virtual testing has been adopted. In order to determine the stiffness of the damaged cross-ply laminate, a classical assumption on the periodicity of the damage pattern is made [13, 45, 67]. For each crack density and local delamination ratio given, a representative periodic cell is defined (Fig. 5.18).

This unit cell represents a cross-ply laminate. The damage occurs only in the central 90° ply. The behavior of the ply is described by a transverse-isotropic

Fig. 5.18 Definition of the equivalent stiffness tensor as a function of the thickness h and of the damage parameters of the ply ($\rho = \frac{\bar{\rho}}{h}, \mu = h\frac{\bar{\mu}}{\bar{\rho}}$)
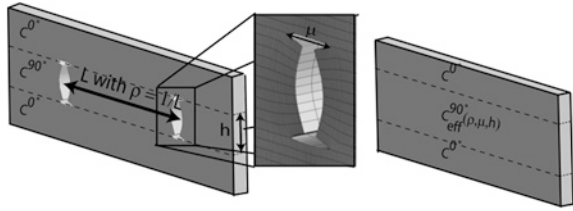
elastic behavior. The six elementary strain components are applied to this representative cell and the stiffness of the laminate is defined by the average of the stress field over this cell. By assuming that the laminate stiffness evolution is only due to the loss of stiffness in the 90° ply, an equivalent stiffness of the damaged ply can be identified by a homogenization approach. The effects of the normalized crack density $\bar{\rho}$ and the associated local delamination ratio $\bar{\mu}$, obtained through the virtual test campaign on the damage compliance tensor $\underset{\approx}{\tilde{S}}$ of the damage ply, can be fitted with the following proposed analytical formulations

$$
\begin{cases}
\underset{\approx}{\tilde{S}} = \underset{\approx}{S}^o + \Delta\underset{\approx}{S}(\bar{\rho},\bar{\mu}) \\
\underset{\approx}{S}(\bar{\rho},\bar{\mu}) = \bar{\rho}\underset{\approx}{H}^a + \frac{\bar{\mu}}{1+\bar{\mu}}\underset{\approx}{H}^b + \bar{\rho}^2\underset{\approx}{H}^c + \bar{\rho}\frac{\bar{\mu}}{1+\bar{\mu}}\underset{\approx}{H}^d
\end{cases}
\tag{5.21}
$$

in which, $\underset{\approx}{S}^o$ is the initial compliance tensor of the ply and $\underset{\approx}{H}^a$, $\underset{\approx}{H}^b$, $\underset{\approx}{H}^c$ and $\underset{\approx}{H}^d$ are the damage effect tensors identified through the virtual test campaign. It is worth mentioning that, in order to simplify the identification procedure and especially to guarantee a positive–definite compliance tensor, the effect tensors are assumed diagonal.

In a second step, it is necessary to propose an evolution law for each damage mechanism. In long fiber composite materials, it is now well established that the thickness of the damaged plies is an important parameter [13]. In fact, the damage threshold and the evolution of transverse crack density are a function of the ply thickness (the thicker the ply is, the lower the damage threshold and the higher the kinetics are). The damage kinetics are thus given by the following relations

$$
\begin{cases}
\bar{\rho} = h(1 - \bar{\mu})\left[\alpha_I\langle y_I - y_I^o\rangle_+^n + \alpha_{II}\langle y_{II} - y_{II}^o\rangle_+^n + \alpha_{III}\langle y_{III} - y_{III}^o\rangle_+^n\right] \\
\bar{\mu} = \langle a_h\bar{\rho}^2 + hb_h\bar{\rho}\rangle_+ \\
\dot{\bar{\rho}} \geq 0
\end{cases}
\tag{5.22}
$$

where y_I, y_{II} and y_{III} are the driving forces and h is the thickness of the ply. α_I, α_{II}, α_{III} and n are material parameters. y_I^o, y_{II}^o and y_{III}^o are the damage thresholds. a_h and b_h are material parameters which permit to have an explicit formulation of the local delamination ratio ($\bar{\mu}$) as a function of the crack density ($\bar{\rho}$). The use of this explicit formulation avoids the definition of a specific evolution law [35] for the local delamination ratio. Moreover, the local delamination tends to slow down the kinetics of the transverse cracking.

The driving forces are expressed in Eq. 5.23 and depend on the positive part of the stress tensor [39] in order to predict damage for tensile loading or even for combined low transverse compression loading and high shear loading.

$$
\begin{cases}
y_I = \sigma_2^+ \tilde{S}_{22} \sigma_2 \\
y_{II} = \sigma_6^+ \tilde{S}_{66} \sigma_6 \\
y_{III} = \sigma_4^+ \tilde{S}_{44} \sigma_4
\end{cases}
\tag{5.23}
$$

where indexes 2 correspond to the in-plane transverse stress components, 6 to in-plane shear components and 4 to the out-of-plane ones. The matrix cracking thresholds are defined by using a coupled criterion [35, 46, 49] which implies that the onset of transverse cracking needs to fulfill two criteria, a stress criterion corresponding to the onset of damage at fiber/matrix scale and an energy criterion to ensure the propagation through the entire ply thickness of the transverse crack. These matrix cracking thresholds are then defined by the following expressions

$$
y_i^o = \max\left[\frac{y_i^{oE}}{h}, y_i^{o\sigma} \right] \quad \text{with } i = I, II, III
\tag{5.24}
$$

in which, y_I^{oE}, y_{II}^{oE} and y_{III}^{oE} are the energy thresholds and $y_I^{o\sigma}$, $y_{II}^{o\sigma}$ and $y_{III}^{o\sigma}$ the stress ones. The energy thresholds are material parameters and the stress ones are the driving forces calculated when the in-plane interfiber criterion, defined in Eq. 5.25, is first fulfilled.

$$
\begin{cases}
\left(\frac{\sigma_{22}}{Y_t}\right)^2 + \left(\frac{\tau_{12}}{S_{12}}\right)^2 + \left(\frac{\tau_{23}}{S_{23}}\right)^2 = 1 & \text{if } \sigma_{22} \geq 0 \\
\left(\frac{\tau_{12}}{S_{12}}\right)^2 + \left(\frac{\tau_{23}}{S_{23}}\right)^2 = 1 & \text{if } \sigma_{22} < 0
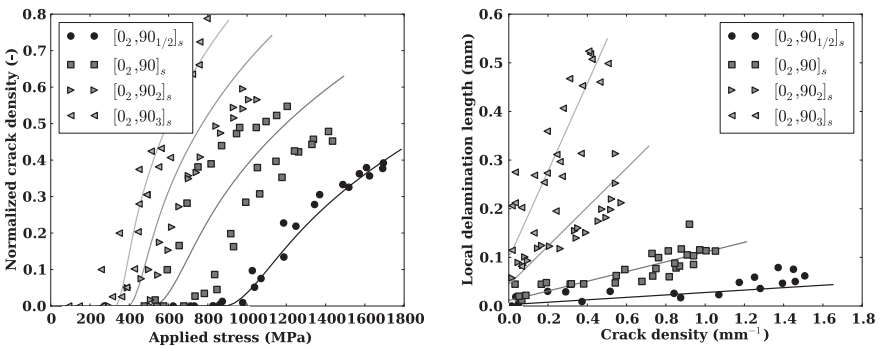\end{cases}
\tag{5.25}
$$

Fig. 5.19 Evolution of the normalized crack density as a function of the applied stress and of the average local delamination length as a function of the crack density for several cross-ply laminates (*in symbols*) and comparison with the prediction of the damage ply behavior (*continuous lines*)

where Y_t, S_{12} and S_{23} are respectively the transverse tensile strength, the in-plane shear strength and the out-of-plane shear strength in the 2-3 plane for a thick UD ply.

Figure 5.19 presents a comparison between the response of the proposed model and the experimental data for T700GC/M21 carbon/epoxy cross-ply laminates with different 90° ply thicknesses. The transverse cracking evolution of the $[0_2/90/0_2]$ laminate is used for the identification of the model parameters (the energy threshold y_I^{oE} and α_1). The results on the other stacking sequences are used to validate the model (see the parameter values in Table 5.1).

5.3.3 Damage Evolution Law of Delamination Including the Intralaminar Damage Effect

Section 5.2 has demonstrated the influence of ply damage on the onset of delamination cracks and its evolution using experimental data. Even if the identification of this influence is difficult using an established procedure, it seems important to take it into account during the design analysis for the sake of security. Several approaches have been proposed in order to take into account this inter/intralaminar coupling. Ladevèze et al. [45] have developed an approach based on virtual testing in order to define relations between the damage state of the laminate (transverse matrix cracking, local delamination, delamination) and their effects on the out-of-plane part of the laminate behavior (micro-meso bridge approach). Abisset et al. [1] and Daghia and Ladevèze [23] derived from the precedent approach a simple expression for the coupling between delamination and matrix cracking. Abisset et al. [1] applied this expression to predict the rupture of open-hole plates and laid emphasis on the requirement of inter/intralaminar coupling.

From our point of view, the expression of the damage evolution (intralaminar or interlaminar) can not be only deduced from virtual testing and a phenomenological approach must be preferred. Nevertheless, the experimental data presented in Sect. 5.2 only demonstrate the influence of the intralaminar damage on the delamination crack evolution law. Due to the scattering of the experimental results, several assumptions could be made for modeling such a coupling. The first one assumes that the damage variable at the interface (λ defined in Eq. 5.2) and the local delamination ratio ($\overline{\mu}$ defined in Sect. 5.3.2) have the same effect on the interface constitutive law. Under this assumption, it becomes possible to define an effective interface damage variable λ^{eff} as [34]

$$\lambda^{\text{eff}} = \min(\lambda + \overline{\mu}, 1) \tag{5.26}$$

The second assumption adopted by Vandellos et al. [72] and Laurin et al. [46] is based on a geometrical point of view. The local delamination ratio being defined as the total length of the local delamination cracks due to matrix cracking

divided by the total length of the interface, this damage variable could be assimilated to a diffuse damage variable and its effect on the strength of the interface could be defined as

$$
\begin{cases}
Z_t^{\overline{\mu}} = (1 - \gamma_\sigma^{\overline{\mu}} \overline{\mu}) Z_t \\
S_{13c}^{\overline{\mu}} = (1 - \gamma_\sigma^{\overline{\mu}} \overline{\mu}) S_{13c} \\
S_{23c}^{\overline{\mu}} = (1 - \gamma_\sigma^{\overline{\mu}} \overline{\mu}) S_{23c}
\end{cases}
\tag{5.27}
$$

where $Z_t^{\overline{\mu}}$, $S_{13c}^{\overline{\mu}}$ and $S_{23c}^{\overline{\mu}}$ are the effective interfacial strengths due to the presence of local delaminations at the interface. A similar assumption could be adopted for the propagation law but in order to avoid numerical convergence difficulties, the effective toughnesses $G_{ic}^{\overline{\mu}}$ with $i = I, II, III$ are so defined that the ratio between δ_0 and δ_f (Eq. 5.7) remains constant. Consequently, the effective interfacial toughnesses have the following expressions

$$
G_{ic}^{\overline{\mu}} = (1 - \gamma_\sigma^{\overline{\mu}} \overline{\mu})^2 G_{ic} \quad \text{with } i = I, II, III
\tag{5.28}
$$

$\gamma_\sigma^{\overline{\mu}}$ in Eqs. 5.27 and 5.28 is a material parameter to be identified and which describes the influence of the intralaminar damage on the interlaminar damage. In the following, the second assumption has been chosen in order to investigate the influence of the parameter identification on the selected application test case.

5.3.4 Implementation in a Finite Element Code

The cohesive zone model and the damage constitutive law of the ply described in the previous sections have been implemented in the implicit finite element solver Zébulon [75]. In order to avoid mesh dependencies due to the damage constitutive law of the ply, a regularization technique is required. Several methods are available [2, 30] but in order to avoid the development of a specific finite element formulation (by a non local approach), the delay effect method has been used. Then, the evolution of the damage variable is defined by a first order ordinary differential equation

$$
\frac{d\overline{\rho}}{dt} = \frac{1}{\tau_c} (F(y_I, y_{II}, y_{III}) - \overline{\rho})
\tag{5.29}
$$

where $F(y_I, y_{II}, y_{III})$ represents the normalized crack density without regularization defined as

$$
\begin{aligned}
F(y_I, y_{II}, y_{III}) = h(1 - \overline{\mu}) \Big[&\alpha_I \langle y_I - y_I^o \rangle_+^n + \alpha_{II} \langle y_{II} - y_{II}^o \rangle_+^n \\
&+ \alpha_{III} \langle y_{III} - y_{III}^o \rangle_+^n \Big]
\end{aligned}
\tag{5.30}
$$

Taking into account the coupling between the intralaminar damage and the inter-laminar damage in a standard finite element code is not straightforward. In order to transfer the damage state information, i.e. in the present case, the local delamination ratio from the neighboring plies to the interface, several methods are also available, such as the non local approach [34]. Nevertheless, as mentioned previously, this type of method requires the development of a non local finite element formulation and could lead to some difficulties for the numerical convergence of the analysis. In this respect, a post increment method has been adopted. The effect of the local delamination ratio on delamination is then computed at the end of each increment, once the convergence at the global scale is ensured. For each Gauss point in cohesive elements, the maximum of the local delamination ratio computed on the two neighboring plies is retained in Eq. 5.27.

5.4 Application on Structural Test Cases

Tensile tests on T300/914C graphite/epoxy double-edge-notched (DEN) cross-ply laminates specimens were experimentally performed by Kortschot and Beaumont [40–42]. The tests were performed on $[90_j/0_j]_{ns}$ laminates (with $j = 1, 2$ and $n = 1, 2, 4$). Moreover, several ratios of total notch length to specimen width, 2a/w, were studied. The specimens tested in tension were radiographed during the mechanical tests. Every radiograph has shown a similar cracking pattern where three main forms of damage are visible: (i) splits in the 0° plies from the tips of the notches, (ii) transverse matrix cracks in the 90° plies and (iii) triangular delamination zones at the 0/90 interfaces.

Due to the presence of intralaminar damage and delamination cracks close to the notches, subjecting DEN specimens to tensile loading seems to be a well adapted test in order to demonstrate the capabilities of the proposed models to describe the influence of intralaminar damages on delamination. The dimensions of the DEN specimens have been chosen as indicated in Fig. 5.20, provided that the 2a/w ratio is equal to 0.5. Moreover, the stacking sequence $[90/0]_s$ has been chosen with 0.125 mm for ply thickness, as indicated in [42].

Using the geometrical and material symmetries, the finite element model of the DEN specimen under tension loading is based on 1/8 of the $[90/0]_s$ specimen

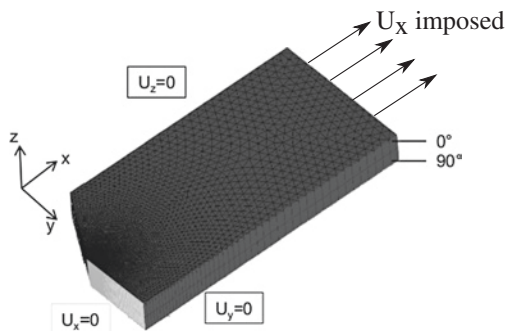**Fig. 5.20** Dimensions of the DEN specimen
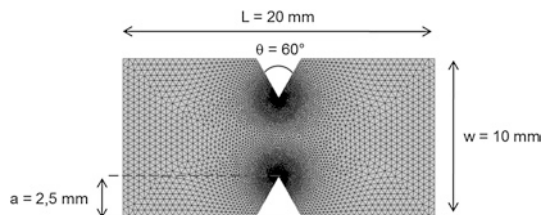
Fig. 5.21 Finite element model of the DEN specimen under tension loading

(Fig. 5.21). Each ply is represented by linear solid elements, with one element through the thickness, and cohesive zone elements are inserted between each ply.

The models used in this work have not been identified on T300/914C laminates but on T700GC/M21 laminates. Therefore, the comparison between the simulations and the experimental observations, reported in [42], will be only qualitative. The material properties used for the simulation are given in Table 5.1. It is important to note that the characteristic time τ_c, used as a delay effect on the damage evolution law of the model (Eq. 5.29), is considered in this work as a numerical parameter which permits to avoid the dependence between the damage rate and the mesh size. For the tensile tests on DEN specimens, simulations in displacement controlled mode with a loading rate of 0.1 mm/min performed with several mesh sizes have shown that the value $\tau_c = 80$ s is satisfying to avoid this numerical dependence.

In order to understand (i) the effect of the behavior of the plies on the interface and (ii) the necessity to take into account the influence of intralaminar damages
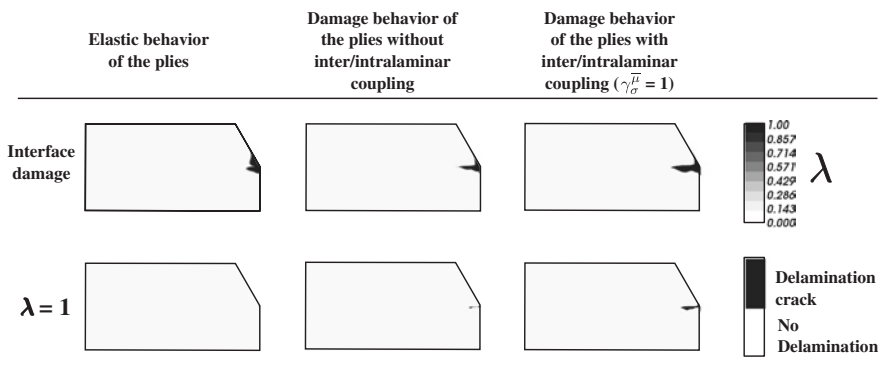

Fig. 5.22 Influence of the ply behavior and of the inter/intralaminar coupling on the delamination zone (interface damage field λ) and on the broken zone ($\lambda = 1$) in the DEN coupon subjected to tension loading
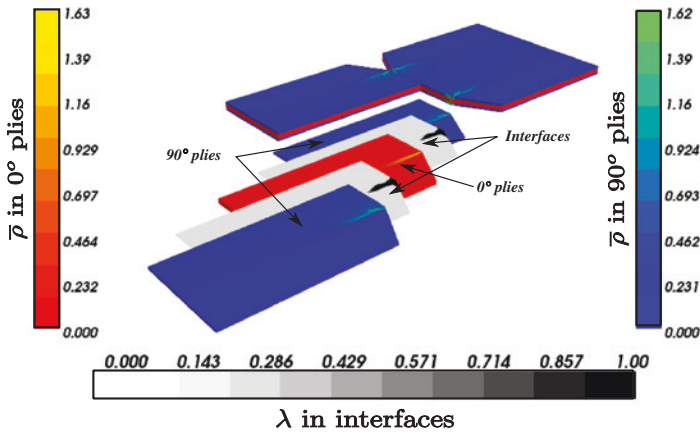
Fig. 5.23 Damage variable fields in the plies ($\overline{\rho}$) and in the interfaces (λ) in the DEN coupon subjected to tension loading for the configuration with a damage model for the plies and inter/intralaminar coupling ($\gamma_\sigma^{\overline{\mu}} = 1$)
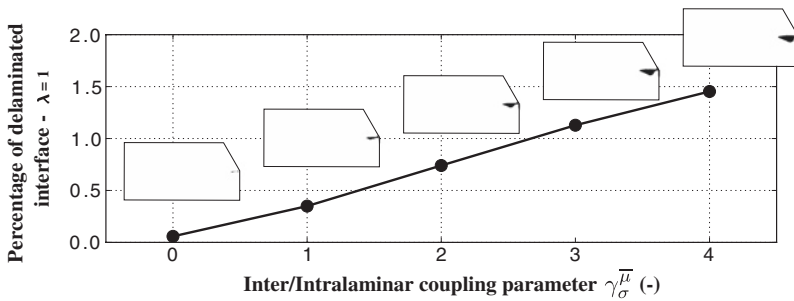

Fig. 5.24 Influence of the inter/intralaminar coupling parameter on the evolution of the percentage of delaminated area in the interfaces in a DEN coupon subjected to tension loading ($\gamma_\sigma^{\overline{\mu}} = 0, 1, 2, 3$ and 4)

on the delamination (i.e. the inter/intralaminar coupling), three configurations have been studied

- without damage model for the plies,
- with damage model for the plies but without inter/intralaminar coupling,
- with the inter/intralaminar coupling in the finite element model.

On the one hand, the comparison between the first two configurations (Fig. 5.22) shows that the ply damage contributes strongly to the propagation of the delamination crack, whose orientation corresponds to the direction of the splits in the 0

plies. Nevertheless, the broken zone (i.e. the delamination zone where the damage variable λ reaches 1) is very localized. In contrast, the last configuration (Figs. 5.22 and 5.23) demonstrates that the inter/intralaminar coupling is essential in order to create a triangular delamination zone at the 0/90 interface, as observed experimentally in [42]. Therefore, it seems crucial to take into account the influence of the intralaminar damage on the delamination and the modeling strategy used in this work appears satisfying to describe this influence. It is worth mentioning that several simulations have been performed in order to chose the increment of time giving a description of the delamination independent of the post increment coupling method used.

On the other hand, the identification of the parameter $\gamma_\sigma^{\overline{\mu}}$ used for the inter/intralaminar coupling appears very important. Indeed, with the last configuration, simulations of the DEN specimen under tensile loading have been performed with $\gamma_\sigma^{\overline{\mu}} = 0, 1, 2, 3$ and 4. The results presented in Fig. 5.24 demonstrate that the size and shape of the broken zone strongly increase when $\gamma_\sigma^{\overline{\mu}}$ becomes higher. Therefore, it seems essential to identify precisely the relation between the interfacial properties and the intralaminar damages, using for instance the experimental characterization procedures proposed in Sect. 5.2.

5.5 Conclusions

In the present chapter, the influence of the intralaminar damage (transverse matrix cracking and local delamination) on the interlaminar damage has been investigated. Using specific device setups and coupons, this influence has been demonstrated experimentally through the analysis of the onset and propagation of delamination cracks. In order to model this inter/intralaminar damage coupling, a cohesive zone model has been developed. It takes into account the local delamination ratio, determined by a continuum damage model in the plies adjacent to the interface, using a post increment method in the implicit finite element analysis. The local delamination ratio is used to decrease the interfacial strength and the fracture toughness of the interface. The application of these models on a double-edge-notched specimen under tensile loading clearly demonstrates the importance of the contribution of the introduced coupling on damage pattern which is very similar to the coupling experimentally observed and reported in Refs. [40–42]. It is worth mentioning that the simulation results are very sensitive to the coupling parameter value, thus implying an improvement in its identification procedure.

References

1. Abisset, E., Daghia, F., Ladevèze, P.: On the validation of a damage mesomodel for laminated composites by means of open-hole tensile tests on quasi-isotropic laminates. Compos. Part A Appl. Sci. Manuf. **42**, 1515–1524 (2011)
2. Allix, O., Deu, J.F.: Delayed-damage modelling for fracture prediction of laminated composites under dynamic loading. Eng. Trans. Rozprawy Inzynierskie **45**(1), 29–46 (1997)
3. Allix, O., Ladevèze, P.: Interlaminar interface modeling for the prediction of laminate delamination. Compos. Struct. **22**, 235–242 (1992)
4. Allix, O., Ladevèze, P., Corigliano, A.: Damage analysis of interlaminar fracture specimens. Compos. Struct. **31**, 61–74 (1995)
5. Allix, O., Lévêque, D., Perret, L.: Identification and forecast of delamination in composite laminates by an interlaminar interface model. Compos. Sci. Technol. **58**(5), 671–678 (1998)
6. Andersons, J., Knig, M.: Dependence of fracture toughness of composite laminates on interface ply orientations and delamination growth direction. Compos. Sci. Technol. **64**, 2139–2152 (2004)
7. ASTM (1994) Standard test method for mode I interlaminar fracture toughness of unidirectional continuous fiber reinforced composite materials. D5528-94A, Philadelphia, PA
8. ASTM (2001) Standard test method for mixed mode I-mode II interlaminar fracture toughness of unidirectional fiber-reinforced polymer matrix composites. D6671-01
9. ASTM (2006a) Standard test method for measuring the curved beam strength of fibre reinforced polymer matrix composite. D6415/D6415M-06a
10. ASTM (2006b) Standard test method for short-beam strength of polymer matrix composite materials and their laminates. D2344/D2344M-00
11. Barenblatt, G.: Mathematical theory of equilibrium cracks in brittle failure. Adv. Appl. Mech. **7**, 55–129 (1962)
12. Benzeggagh, M., Kenane, M.: Measurement of mixed-mode delamination fracture toughness of unidirectional glass/epoxy composites with mixed-mode bending apparatus. Compos. Sci. Technol. **56**, 439–449 (1996)
13. Berthelot, J.M.: Transverse cracking and delamination in cross-ply glass-fiber and carbon-fiber reinforced plastic laminates: Static and fatigue loading. Appl. Mech. Rev. **56**(1), 111–147 (2003)
14. Blackman, B., Kinloch, A.: Fracture tests for structural adhesive joints. In: Moore, D., Pavan, A., Williams, J. (eds.) Fracture Mechanics Testing Methods for Polymers, Adhesives and Composites, pp. 225–270. Elsevier, Amsterdam (2001)
15. Caiazzo, A., Costanzo, F.: Modeling the constitutive behavior of layered composites with evolving cracks. Int. J. Solid Struct. **38**(20), 3469–3485 (2001)
16. Camanho, P., Dávila, C., de Moura, M.: Numerical simulation of mixed-mode progressive delamination in composite materials. J. Compos. Mater. **37**(16), 1415–1438 (2003)
17. Carlsson, L., Gillepsie, J., Pipes, R.: On the analysis and design of the end notched flexure (ENF) specimen for mode II testing. J. Compos. Mater. **20**, 594–604 (1986)
18. Charrier, J., Carrère, N., Laurin, F., Bretheau, T., Goncalves-Novo, E., Mahdi, S.: Proposition of 3D progressive failure approach and validation on tests cases. In: 14th European Conference on Composite Materials (ECCM/14) (2010)
19. Charrier, J., Carrère, N., Laurin, F., Goncalves-Novo, E., Mahdi, S.: Proposition d'une méthode d'analyse dédiée aux structures composites soumises à des sollicitations hors-plan. In: 17ème Journées Nationales sur les Composites (JNC 17) (2013)
20. Choi, N., Kinloch, A., Williams, J.: Delamination fracture of multidirectional carbon-fiber/epoxy composites under mode I, mode II and mixed-mode I/II loading. J. Compos. Mater. **33**, 73–100 (1999)

21. Crews, J., Reeder, J.: A mixed-mode bending apparatus for delamination testing. Technical report, Langley Research Center, Virginia, USA (1988)
22. Cui, W., Wisnom, M., Jones, M.: A comparison of failure criteria to predict delamination of unidirectional glass/epoxy specimens waisted through the thickness. Composites **23**(3), 158–166 (1992)
23. Daghia, F., Ladevèze, P.: Identification and validation of an enhanced mesomodel for laminated composites within the WWFE-III. J. Compos. Mater. **47**(20–21), 2675–2693 (2013). doi:10.1177/0021998313494095. URL http://jcm.sagepub.com/content/47/20-21/2675
24. Daudeville, L., Ladevèze, P.: A damage mechanics tool for laminate delamination. Compos. Struct. **25**, 547–555 (1993)
25. Dávila, C., Camanho, P., Turon, A.: Effective simulation of delamination in aeronautical structures using shells and cohesive elements. J. Aircr. **45**, 663–672 (2008)
26. de Morais, A., Pereira, A.: Mixed-mode I + II interlaminar fracture of glass/epoxy multidirectional laminates—part 1: analysis. Compos. Sci. Technol. **66**, 1889–1895 (2006)
27. de Morais, A., Pereira, A.: Application of the effective crack method to mode I and mode II interlaminar fracture of carbon/epoxy unidirectional laminates. Compos. Part A Appl. Sci. Manuf. **38**, 785–794 (2007)
28. de Morais, A., de Moura, M., Marques, A., de Castro, P.: Mode I interlaminar fracture of carbon/epoxy cross-ply composites. Compos. Sci. Technol. **62**, 679–686 (2002)
29. Dugdale, D.: Yielding of steel sheets containing slits. J. Mech. Phys. Solids **8**, 100–104 (1960)
30. Germain, N., Besson, J., Feyel, F.: Composite layered materials: anisotropic nonlocal damage models. Comput. Method Appl. Mech. **196**(4144), 4272–4282 (2007). doi:10.1016/j.cma.2007.04.009. URL http://www.sciencedirect.com/science/article/pii/S004578250700182X
31. Gong, X., Benzeggagh, M.: Mixed mode interlaminar fracture toughness of unidirectional glass/epoxy composite. In: Composite Materials: Fatigue and Fracture, vol. 5, pp. 100–123. ASTM STP 1230 (1995)
32. Guinard, S., Allix, O., Guédra-Degeorges, D., Vinet, A.: A 3D damage analysis of low-velocity impacts on laminated composites. Compos. Sci. Technol. **62**, 585–589 (2002)
33. Hinton, M., Kaddour, A., Soden, P.: Failure Criteria in Fibre Reinforced Polymer Composites: The World-Wide Failure Exercise. Elsevier Science Ltd., Oxford (2004)
34. Huchette, C., Guinot, F.: Experimental and numerical analysis on delamination growth in damaged composite material. In: 13th European Conference on Composite Materials (ECCM/13) (2008)
35. Huchette, C., Lévêque, D., Carrère, N.: A multiscale damage model for composite laminate based on numerical and experimental complementary tests. In: Sadowski, T. (ed.) IUTAM Symposium on Multiscale Modelling of Damage and Fracture Processes in Composite Materials, No. 135 in Solid Mechanics and Its Applications, pp. 241–248. Springer, Netherlands (2006). URL http://link.springer.com/chapter/10.1007/1-4020-4566-2_28
36. Huchette, C.: Sur la complémentarité des approches expérimentales et numériques pour la modélisation des mécanismes d'endommagement des composites stratifiés. Ph.D. thesis, University of Paris VI—Pierre et Marie Curie, France (2005)
37. ISO (1987) Adhesives—determination of Tensile Strength of Butt Joints. ISO 6922
38. Jackson, W., Ifju, P.: Through-the-thickness tensile strength of textile composites. Composite materials: testing and design 12, ASTM STP 1274, 218–238 (1996)
39. Ju, J.: On energy-based coupled elastoplastic damage theories: constitutive modeling and computational aspects. Int. J. Solids Struct. **25**, 803–833 (1989)
40. Kortschot, M., Beaumont, P.: Damage mechanics of composite materials. I: a damage based notched strength model. Compos. Sci. Technol. **39**, 289–301 (1990)
41. Kortschot, M., Beaumont, P.: Damage mechanics of composite materials. II: measurements of damage and strength. Compos. Sci. Technol. **39**, 303–326 (1990)
42. Kortschot, M., Beaumont, P., Ashby, M.: Damage mechanics of composite materials. III: prediction of damage growth and notched strength. Compos. Sci. Technol. **40**, 147–165 (1991)

43. Krueger, R.: The virtual crack closure technique: history, approach and applications. Technical report, ICASE, Hampton, Virginia (2002)
44. Ladevèze, P., LeDantec, E.: Damage modelling of the elementary ply for laminated composites. Compos. Sci. Technol. **43**(3), 257–267 (1992). doi:10.1016/0266-3538(92)90097-M. URL http://www.sciencedirect.com/science/article/pii/026635389290097M
45. Ladevèze, P., Lubineau, G., Marsal, D.: Towards a bridge between the micro- and meso-mechanics of delamination for laminated composites. Compos. Sci. Technol. **66**, 698–712 (2006)
46. Laurin, F., Carrère, N., Huchette, C., Maire. J.F.: A multiscale hybrid approach for damage and final failure predictions of composite structures. J. Compos. Mater **47**(20–21), 2713–2747 (2013). doi:10.1177/0021998312470151. URL http://jcm.sagepub.com/content/47/20-21/2713
47. Laurin, F., Carrère, N., Maire, J.F.: A multiscale progressive failure approach for composite laminates based on thermodynamical viscoelastic and damage models. Compos. Part A Appl. Sci. Manuf. **38**, 198–209 (2007)
48. Laurin, F., Charrier, J.S., Lévêque, D., Maire, J.F., Mavel, A., Nunez, P.: Determination of the properties of composite materials thanks to digital image correlation measurements. Procedia IUTAM **4**, 106–115 (2012)
49. Leguillon, D.: Strength or toughness? A criterion for crack onset at a notch. Eur. J. Mech. A-Solid **21**, 61–72 (2002)
50. Lekhnitskii, S.G.: Theory of Elasticity of an Anisotropic Elastic Body. Holden-Day Edn. Inc., San Francisco (1963)
51. NASA.: Standard tests for toughened resin composites. Technical report, Langley Research Center, Virginia, USA (1982)
52. O'Brien, T.: Mixed-mode strain energy-release rate effects on edge delamination of composites. In: 836 AS (ed.) Effects of Defects in Composite Materials. American Society for Testing and Materials, pp. 125–142 (1984)
53. Olsson, R.: Review—a survey of test methods for multiaxial and out-of-plane strength of composite laminates. Compos. Sci. Technol. **71**, 773–783 (2011)
54. Ozdil, F., Carlsson, L.: Beam analysis of angle-ply laminate DCB specimens. Compos. Sci. Technol. **59**, 305–315 (1999)
55. Pereira, A., de Morais, A.: Mixed-mode I + II interlaminar fracture of glass/epoxy multidirectional laminates—part 2: experiments. Compos. Sci. Technol. **66**, 1896–1902 (2006)
56. Pereira, A., de Morais, A.: Mixed-mode I + II interlaminar fracture of carbon/epoxy laminates. Compos. Part A Appl. Sci. Manuf. **39**, 322–333 (2008)
57. Pereira, A., de Morais, A.: Mixed-mode I+III interlaminar fracture of carbon/epoxy laminates. Compos. Part A Appl. Sci. Manuf. **40**, 518–523 (2009)
58. Pinho, S., Iannucci, L., Robinson, P.: Formulation and implementation of decohesion elements in an explicit finite element code. Compos. Part A Appl. Sci. Manuf. **37**, 778–789 (2006)
59. Prombut, P.: Caractâ€šrisation de la propagation de délaminage des stratifiés composites multidirectionnels. Ph.D. thesis, University of Toulouse III—Paul Sabatier, France (2007)
60. Prombut, P., Michel, L., Lachaud, F., Barrau, J.J.: Delamination of multidirectional composite laminates at 0/± ply interfaces. Eng. Fract. Mech. **73**, 2427–2442 (2006)
61. Reeder, J., Crews, J.: Mixed-mode bending method for delamination testing. AIAA J. **28**, 1270–1276 (1990)
62. Reeder, J., Crews, J.: Redesign of the mixed-mode bending delamination test to reduce non-linear effects. J. Compos. Technol. Res. **14**, 12–19 (1992)
63. Reeder, J.: An evaluation of mixed-mode delamination failure criteria. Technical report, Langley Research Center, Virginia, USA (1992)
64. Schuecker, C., Davidson, B.: Evaluation of the accuracy of the four-point bend end-notched flexure test for mode II delamination toughness determination. Compos. Sci. Technol. **60**, 2137–2146 (2000)

65. Sun, C., Zheng, S.: Delamination characteristics of double-cantilever beam and end-notched flexure composite specimens. Compos. Sci. Technol. **56**, 451–459 (1996)
66. Talreja, R.: Stiffness properties of composite laminates with matrix cracking and interior delamination. Eng. Fract. Mech. **25**(5), 751–762 (1986)
67. Thionnet, A., Renard. J.: Meso-macro approach to transverse cracking in laminated composites using Talreja's model. Compos. Eng. **3**(9), 851–871 (1993). doi:10.1016/0961-9526(93)90044-K. URL http://www.sciencedirect.com/science/article/pii/096195269390044K
68. Turon, A.: Simulation of delamination in composites under quasi-static and fatigue loading using cohesive zone models. Ph.D. thesis, Department d'Enginyeria Mecánica i de la Construcció Industrial, Universitat de Girona, Spain (2006)
69. Turon, A., Dávila, C., Camanho, P., Costa, J.: An engineering solution for mesh size effects in the simulation of delamination using cohesive zone models. Eng. Fract. Mech. **74**, 1665–1682 (2007)
70. Turon, A., Camanho, P., Costa, J., Renart, J.: Accurate simulation of delamination growth under mixed-mode loading using cohesive elements: definition of intralaminar strengths and elastic stiffness. Compos. Struct. **92**, 1857–1864 (2010)
71. Vandellos, T., Hautier, M., Carrère, N., Huchette, C.: Development of a new fracture test to identify the critical energy release rate: the tensile flexure test on notched specimen. Eng. Fract. Mech. **96**, 641–655 (2012)
72. Vandellos, T., Huchette, C., Carrère, N.: Proposition of a framework for the development of a cohesive zone model adapted to carbon-fiber reinforced plastic laminated composites. Compos. Struct. **105**, 199–206 (2013)
73. Whitcomb, J.: Analysis of instability-related growth of a through-width delamination. Technical report, Langley Research Center, Virginia, USA (1984)
74. Wisnom, M., Hallett, S.: The role of delamination in strength, failure mechanism and hole size effect in open hole tensile tests on quasi-isotropic laminates. Compos. Part A Appl. Sci. Manuf. **40**, 335–342 (2009)
75. Zébulon (2014). URL http://www.zset-software.com/products/zebulon/